Feasibility of Implementing the PILATUS3 CdTe 300k Detector as a Real Time Gamma Camera in Intraoperative Medical Imaging

Mariam Andersson

Bachelor's Thesis in Physics

LUND UNIVERSITY

Department of Experimental Particle Physics, Melbourne

Supervised by Dr. Roger Rassool (Melbourne) and Dr. Lennart Isaksson (Lund)

August 2015

Abstract

The full-width-at-half-maximum of the point spread functions for a pixellated cadmium telluride detector exposed to gammas from a 140.5 keV Tc-99m source are modelled in GATE, at a detector-collimator distance of 5 cm, and collimator-source distances of 5 cm and 10 cm, with lead pinholes of diameter 1.0 mm, 1.5 mm, 2.0 mm and 5.0 mm acting as collimators. The PILATUS3 X CdTe 300k detector from Dectris was then used to image a custom phantom with the same set up as in simulations at the Austin hospital in Melbourne, Australia. The exposure time was also varied, with the aim to establish if the detector could be repurposed for applications within medical imaging, more specifically as a gamma camera in guided sentinel lymph node biopsy. Moreover, the quantum efficiency of the detector, hitherto unknown, was calculated. Results found that the 2.0 mm and 5.0 mm would be particularly suited for real time imaging and intraoperative use, with exposure times of 30 s and 5 s resolving 3.0 mm and 8.5 mm respectively. The smaller pinhole sizes achieved resolutions of down to 1 mm with longer exposures of 120 s and 300 s, showing promise for application in single photon emission computed tomography. For both a detector-collimator and collimator-source distance of 5 cm, the simulated spatial resolution was in agreement with the experimental results, validating the use of simulations to model such situations. The CdTe sensor was found to have an intrinsic quantum efficiency of 20.8 ± 0.2 %, confirming its superiority over other semiconductor counterparts such as silicon.

Contents

Abbreviations

SNB – Sentinel Lymph Node Biopsy
SN – Sentinel Node
SNR – Signal-to-Noise Ratio
QE – Quantum Efficiency
GATE – GEANT4 Application for Tomographic Emission
PSF – Point Spread Function
HPD – Hybrid Pixel Detector
PET – Positron Emission Tomography
SPECT – Single Photon Emission Computed Tomography

1 Introduction

1.1 Lymphoscintigraphy and Sentinel Lymph Node Biopsy

Ever since Wilhelm Conrad Röntgen's pioneering production and detection of x-rays in 1895, ionising radiation has played a paramount role in the development of both diagnostic and therapeutic techniques within medicine. One such diagnostic technique is lymphoscintigraphy, in which a radioactive, gamma-emitting, tracer is injected into a region of the body and used to image and localise the lymph vessels and nodes. This is particularly important in sentinel lymph node biopsy (SNB), the primary method used to stage many breast cancers and melanomas [1], and is also becoming standard for certain oral cancers [2, 3].

The sentinel node (SN) is defined as "the lymph node on the direct drainage pathway from the primary tumor" [4]; the spread of cancer occurs through the bloodstream or the lymphatic system, and detection of the cancer in the SN is therefore an indication of potential metastasis [2]. Conversely, the lack of cancer in the SN is a sign that the cancer is confined to a local area, and has not spread. The injected radiotracer most often contains the metastable isotope Tc-99m [5], which predominantly emits photons at an energy of 140.5 keV and has a half-life of 6.01 hours [6]. Lymphoscintigraphy can be conducted preoperatively in order to localise the relevant lymph nodes, or intraoperatively in order to guide surgeons to the SN. Typically, gamma probes are used in combination with a blue dye to identify the nodes [2], but recent innovations have led to dynamic imaging. With dynamic imaging, the surgeon can use a gamma camera, such as the Sentinella 102 from GEM-Imaging equipped with a scintillating CsI crystal, to visualise the real time passage of the radiotracer through the lymphatic system [7]. Doses ranging between 5 MBq to 35 MBq are recommended [8], with commercial radiotracers such as Lymphoseek advising a dose of 18.5 MBq and commencement of imaging between 15 minutes and 15 hours post administration [9].

Given that human lymph nodes can vary in size between 2 mm to 20 mm [10], and are found at varying distances to each other, the spatial resolution of the imaging system – consisting of the detector and a collimator – is of high importance. Also of the utmost importance in real time lymphoscintigraphy, during SNB, is the system sensitivity. Image exposure times must be short enough to fall within the boundaries of 'real time' during a surgery whilst adhering to the recommended doses, but long enough to ensure an adequately high signal-to-noise ratio (SNR) to resolve the lymph nodes. Furthermore, the intrinsic energy resolution of the detector is of great significance; the higher the energy resolution, the lower the noise and the higher the SNR, which is desirable. Semiconductor detectors offer an alternative to the standard scintillators used in gamma cameras – they possess superior energy resolution, can have more compact designs and can boast higher intrinsic spatial resolutions [11].

1.2 Purpose

This report aims to assess the feasibility of implementing the single photon counting PILATUS3 CdTe detector from Dectris in intraoperative, real time guided SNB. The quantum efficiency (QE) of the detector at 140.5 keV is experimentally determined. Simulations in GATE (GEANT4 Application for Tomographic Emission) are performed to model the point spread functions (PSF) of PILATUS3 in combination with single pinhole collimators of diameters 1.0 mm, 1.5 mm, 2.0 mm and 5.0 mm so as to determine theoretical values for the spatial resolutions of the systems. The theoretical values experimentally tested at the Austin Hospital in Melbourne, Australia in conjuction with the EPP laboratory at the University of Melbourne by constructing and imaging a custom phantom filled with a liquid Tc-99m source. Moreover, phantom exposures of different lengths are acquired to investigate whether or not the imaging systems are sensitive enough for intraoperative use. Lastly, the images obtained are binned with three different methods to see if such grouping of the pixels results in improved SNR.

2 Background

2.1 PILATUS3 CdTe

2.1.1 Detector System

The PILATUS3 CdTe used for this project was a PILATUS3 X CdTe 300k, equipped with 487×619 pixels of area $172\,\mu$m $\times 172\,\mu$m and depth $1000\,\mu$m and set to a threshold of 70.25 keV. The pixels are divided into three modules, stacked on top of each other with an inter-module spacing of only 3 pixels. The detector was kept at optimum operating conditions using a water cooling system and a dry air supply from a N_2 cylinder. The programs CamServer and Tvx were used to control the detector and obtain images [12].

2.1.2 Efficiency

The single photon counting PILATUS 3 CdTe detector by Dectris is the first large area detector of its kind to enter the market. The high atomic numbers of the cadmium ($Z = 48$) and telluride ($Z = 52$) in the CdTe sensor lead to a higher photon stopping power when compared with other semiconductor materials such as silicon, enabling a higher quantum efficiency at higher energies. The QE of the detector is a measure of the number of counts registered, N_r, relative to the number of counts incident on the detector surface, N_i.

$$QE = 100\ (\frac{N_r}{N_i}) \tag{1}$$

Figure 1 shows the simulated and measured quantum efficiencies of the cadmium telluride sensor with a thickness of 1000 μm for different photon energies up to 100 keV.

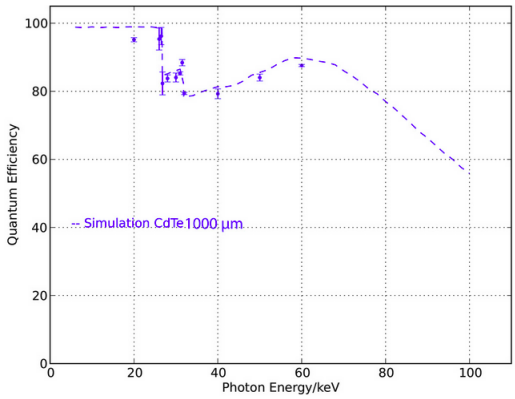

Figure 1: Variation of the PILATUS3 X CdTe quantum efficiency with incident photon energy (sensor of thickness 1000 μm). The dotted line represents simulated values and the data points were obtained by DECTRIS in cooperation with PTB at BESSY. Graph sourced from the Dectris home page [13].

Dectris quotes the QE of an equally thick silicon sensor to be around 20% at 20 keV – a drastic difference from the QE of above 90% for the cadmium telluride sensor [13].

2.1.3 Technology

In semiconductor detectors, a potential difference is applied over two ends of the detecting material. Incoming photons create electron-hole pairs in the sensor, and the charge carriers migrate towards the electrode of opposite charge and generate a pulse, or signal. The higher the energy of the incident photons, the more numerous the electron-hole pairs and the higher the pulse amplitude.

The PILATUS3 CdTe is a hybrid pixel detector (HPD), meaning that each pixel of the CdTe sensor is directly bonded to the read-out electronics. The electronics consist of an amplifier, a discriminator and a

counter. When a photon interacts in the sensor, the subsequent charge pulse is amplified and fed through a discriminator which compares the amplitude of the pulse to that of a pulse at which the threshold energy is set. If the amplitude is too low, the photon energy does not reach that of the threshold and it is not counted. A sufficiently high amplitude triggers the generation of a uniform pulse which is sent to the counter [14]. At high fluxes of incident photons, the pulses generated can "pile up" and lead to paralysation of the counter. As such, all Dectris detectors employ count rate corrections based on "instant retrigger technology". A dead time interval the length of a single photon pulse is defined. At high count rates, pulses are re-evaluated after the dead time interval instead of only being evaluated initially; if the pulse is long enough and above the threshold energy after this interval, it is counted again. This technology yields a possible count rate of over $5 \cdot 10^6$ counts/s/pixel [15].

The small size of the pixels, $172\,\mu$m $\times$ $172\,\mu$m, and their close proximity to the read-out electronics reduces noise and power consumption. Read-out time is fast at under 1 ms and frame rates are as high as 500 Hz. Since detection is direct and digital, PILATUS detectors are effectively free of dark current and readout noise.

2.2 Quantum Efficiency

The concept of QE was introduced in Section 2.1.2 as the ratio of photons registered by the detector, N_r, to photons incident on the detector, N_i (see Equation 1). With PILATUS3, N_r can easily be extracted from the image obtained, but N_i must be calculated. N_i can be calculated with knowledge of the source activity, A, at a certain time, T, and its location relative to the detector. The source emits radiation in all directions; the fraction of this that is incident on the detector surface can be described by the solid angle, Ω. The solid angle has the unit steradians, and has a maximum value of 4π which describes the total area of a sphere.

Figure 2 shows that the area of the projection of an area A onto a sphere centred around a source, S, is represented by the solid angle Ω.

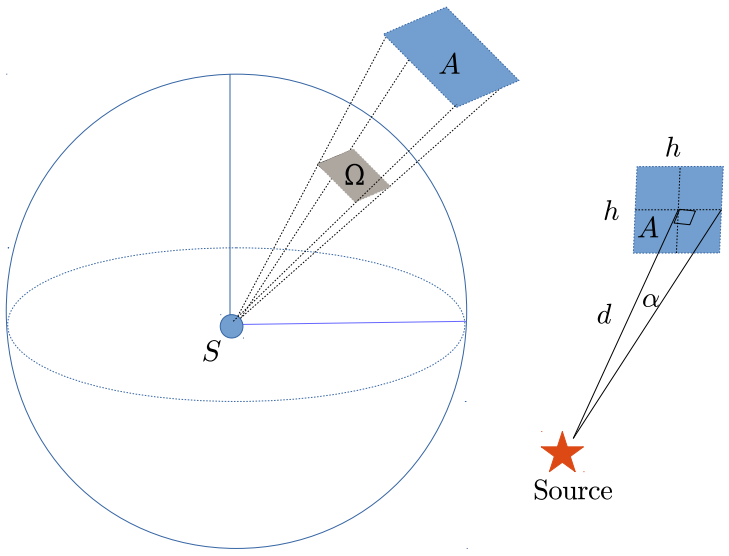

Figure 2: An area, A, is projected onto the surface of a sphere centred around a source, S. The projection relative to the total area of the sphere can be described by the solid angle, Ω. Note that the area represented by Ω is not a square and follows the curvature of the sphere surface. The area, A, has dimensions $h \times h$. d is the perpendicular distance between the source and centre of A.

α is the angle between the pe

The fraction, $\frac{\Omega}{4\pi}$, therefore denotes the fraction of radiation from S that is incident upon the area A. The solid angle for the projection of a square detector active area is given by Equation 2 [16].

$$\Omega = 4 \arcsin(\sin^2 \alpha) \tag{2}$$

where the angle α is defined by Equation 3:

$$\alpha = \arctan(\frac{h}{2d}) \tag{3}$$

and h is the side length of the square active area, and d is the distance from the source to the centre of the active area. Assuming that the source half-life is significantly larger than the duration, t, for which counts are registered, N_i is given by Equation 4.

$$N_i = A(T) \cdot t \cdot \frac{\Omega}{4\pi} \tag{4}$$

2.3 Point Spread Function

The point spread function, PSF, is defined as "the radiation intensity distribution in the image of an infinitely small aperture", and its full width at half maximum (FWHM) is a measure of the intrinsic spatial resolution of the system [17]. The PSF can be modelled by a Gaussian of the form:

$$PSF(x) = a \cdot \exp(\frac{-(x-\mu)^2}{2\sigma^2}) \tag{5}$$

where a describes the height of the distribution, μ is its average and σ is the standard deviation.
The FWHM of the Gaussian is defined as:

$$\text{FWHM} = \sqrt{6 \ln 2} \cdot \sigma \tag{6}$$

2.4 Pinhole Collimators

As mentioned in Section 2.2, it is common for a radioactive source to emit radiation in all directions. This proves problematic when trying to image an object as photons from one small part of the source may hit all parts of the detector, blurring any details. The function of a collimator is to limit the photons reaching the detector such that only the photons travelling in a specific direction and/or from a certain position can be detected. As such, photons from one particular place will only be found in one region on the detector image, reducing blurring and allowing for a more detailed image to be created.

There are many types of collimator, and the simplest possible collimator for radiation of energy 140.5 keV is that of the cylindrical pinhole collimator. The pinhole collimator consists of a hole in a sheet of material of high attenuation coefficient, an example being lead. Figure 3 summarises the key principles of pinhole imaging.

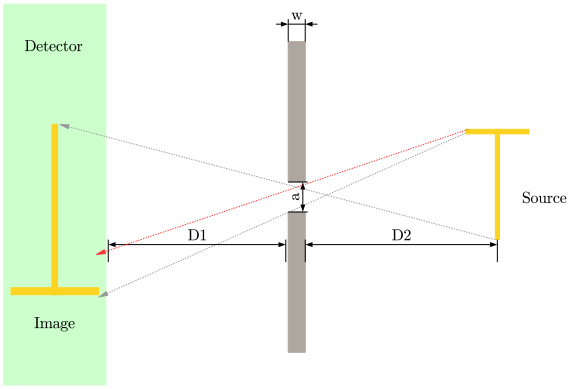

Figure 3: A source/object is imaged through a pinhole of aperture, a, and channel depth, w, on a detector. The dashed grey lines indicate the boundaries of the image. The dashed red line shows how the pinhole can accept photons travelling with a range of different directions from the same source, causing blurring.

The magnification, M, of the image is given by the ratio $\frac{D1}{D2}$. The dashed red line in Figure 3 demonstrates the inherent blurring involved with pinhole imaging; photons from the same point on the source, but travelling in different directions, can both pass through the pinhole and thus cause image blurring to some degree. The blurring can be reduced by increasing the channel depth, w, of the pinhole, or by reducing the aperture size, a. These adjustments, however, reduce the sensitivity of the system, meaning that less photons can pass through and longer exposure times may be needed. Choosing a suitable pinhole aperture involves a trade-off between sensitivity and resolution.

The pinhole resolution, R_p, can be approximated by [20]:

$$R_p = \frac{a}{D1} \cdot (D1 + D2) \tag{7}$$

3 Method

3.1 Point Spread Function Simulations in Gate

The PSFs for different pinhole geometries and source-collimator distances were modelled in GATE (Geant4 Application for Tomographic Emission). GATE is an open source software, developed specifically for Monte Carlo based numerical simulations within medical physics and built upon the Geant4 toolkit. It offers a user-friendly approach to defining detector geometries, source distributions and other simulation parameters relevant to positron emission tomography (PET), single photon emission computed tomography (SPECT) and sctintigraphy. GATE simulations take into account relevant electromagnetic photon-matter interactions such as the photoelectric effect, Compton scattering, Rayleigh scattering and single/multiple scattering [18], and offer both spatial and temporal tracking of particles. Its use has been validated for simulating PSFs with a Tc-99m source, albeit with another type of collimator [19].

A 100 pixel $\times$ 100 pixel CdTe detector with pixels of size $172\,\mu$m $\times$ $172\,\mu$m was built and located 5 cm from a pinhole collimator; it was unnecessary to simulate true size of the detector since this would increase computation time to no advantage since the PSFs would remain the same size regardless. The pinhole was modelled according to the design in Figure 4; the use of two pieces of lead meant that the pinhole size could be easily changed in practise, without disrupting the setup.

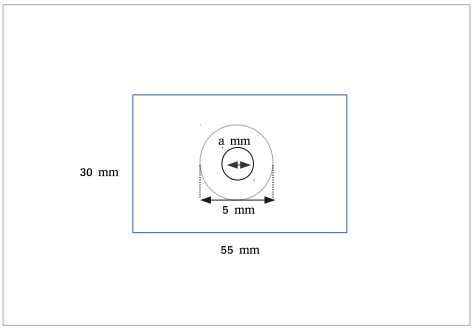

Figure 4: Pinhole consisting of two overlapping lead sheets, a large and a small sheet of thickness 2.16 mm and 1.1 mm respectively. The larger had an aperture of 5 mm and the smaller a variable aperture. Note that the smaller pinhole was not centred on the small lead sheet in practise – only in simulation.

A monoenergetic Tc-99m source of radius 10^{-5} m, initial activity 100 Mbq and energy 140.5 keV was placed at distances of 5 cm and 10 cm from the collimator, emitting in the angle of acceptance of the pinhole to minimise computation time. 100 million photon histories were generated for each simulation. The output from the simulation was a binary file, listing the coordinates of each hit. The binary file was processed in Matlab to visualise the detector images, and also to fit a Gaussian to the PSF so as to determine the FWHM, or spatial resolution, of the system. Figure 5 shows a visualisation of the simulation geometry for the case where a 1 mm pinhole at 10 cm from the source is modelled.

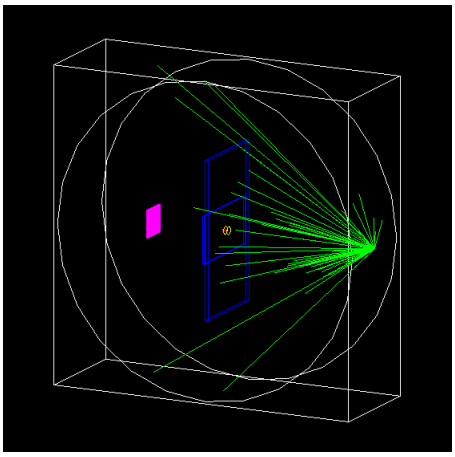

Figure 5: Visualisation of a simulation involving a 1 mm lead pinhole 5 cm from the CdTe detector sensitive area, and 10 cm away from a Tc-99m point source in GATE. The emission angle of the source was modified in order to cover the acceptance angle of the pinhole, but avoid unnecessary emissions to save computation time.

3.2 Masks and Background Measurements

A mask was created to flag any pixels with misrepresentative values to later exclude them from data analysis; this included dead pixels, hot pixels and module gaps. A preliminary mask was made in Tvx by sending 100 pulses to each pixel and excluding the pixels whose counters deviated from this value. Bad pixels were flagged with a value of -1, and the rest were given a value of 1. The mask was then imported into Matlab in

the form of a matrix where the element-wise multiplication of the mask matrix with an image matrix would flag the bad pixels as negative in the image, and exclude them from any data processing.

5 background measurements of 300 s each were taken at the Nuclear Medicine Lab at the Austin hospital in Melbourne, Australia where the experiments were performed. The TIF images generated by PILATUS3 were imported into Matlab, where the Mask was applied to flag bad pixels. Any additional hot pixels were ignored by imposing the condition that pixels with counts over 50 during the 300 s period were also flagged with negative numbers. The counts in the good pixels were summed, and the uncertainty of the summed value was taken as its square root. The background rate (per second, per pixel) for each image was obtained and the values from each image were averaged to $(3.24 \pm 0.02)\,\text{counts/s} \cdot \text{px}$.

For every image later analysed, a mask was applied and the expected background depending on the exposure time was removed from each pixel.

3.3 Phantom Measurements and Binning

A phantom consisting of a rectangular piece of perspex with wells of varying diameter and distance apart was constructed according to the geometry shown in Figure 6.

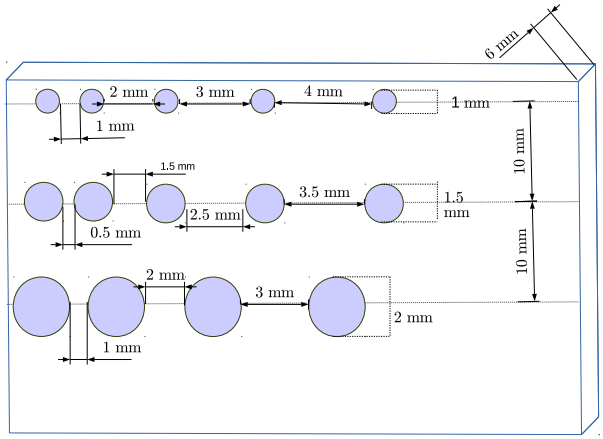

Figure 6: Perspex phantom constructed for resolution tests. The blue circles represent wells that were drilled as far into the perspex (6 mm) as possible, without breaking the surface.

The different sizes of the wells and the varying distances between them was intended to resemble the distribution of radiotracer in the lymphatic system after a longer period of absorption, when several lymph nodes have absorbed the chemical.

Figure 7 shows the setup for the measurements. For every pinhole, the height of the phantom was adjusted so that the image fell on the mid-right sensor of PILATUS3. Lead bricks were built up around the set-up to prevent the emitted gammas from irradiating the surrounding area.

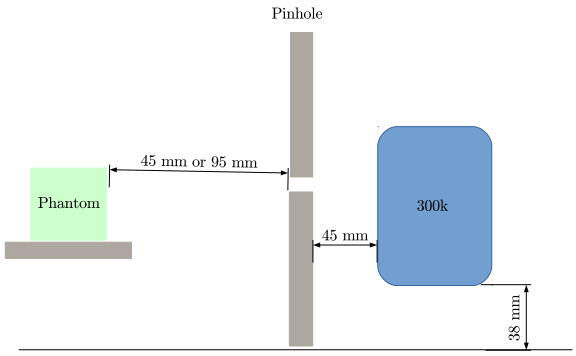

Figure 7: Side view of phantom measurement set up with PILATUS3.

31.4 MBq of Tc-99m was diluted in 140 μl of solution and injected into all phantom wells at 12:57. Image capture commenced at 14:17, when the activity had reached 26.9 MBq. In order to provide a basis for comparison, all later images were standardised to this activity by multiplying the counts by a correction factor, C:

$$C = \exp(\lambda t) \tag{8}$$

where λ is the decay constant of Tc-99m, given by $\lambda = \frac{\ln 2}{T_{\frac{1}{2}}}$, $T_{\frac{1}{2}}$ is the half life of Tc-99m and t is the time between the initial measurement at 14:17 and the time at which the image in question was taken. C describes the relative difference in emission intensity between two different points in time, assuming that the source decays according to the radioactive decay law.

Exposures of different lengths were taken for the different pinholes, ranging from 1 s to 300 s.

The images were imported into Matlab, visualised and also binned into 25-pixel bins using the Matlab 'bin2' function. The binning involved either selecting the mean, median or minimum pixel value from a 5×5 pixel group to represent the whole region, in an attempt to clarify the images.

3.4 Quantum Efficiency Measurements

Figure 8 shows the set up used to obtain data for a determination of the intrinsic detector QE.

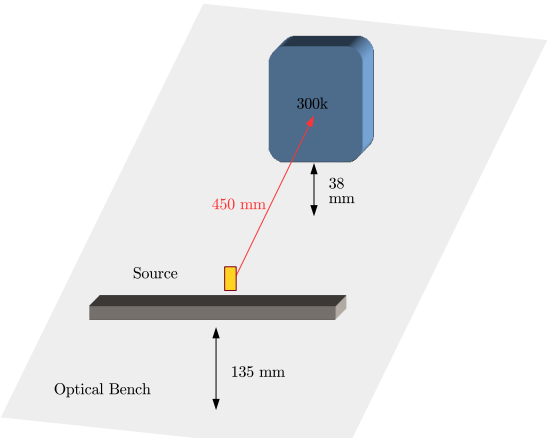

Figure 8: Set up used for measurements on absolute, intrinsic QE of the PILATUS3 CdTe detector. The yellow box represents the source: a vial with a small droplet of Tc-99m solution lying in the bottom. The red arrow is the perpendicular distance of the vial to the centre of the detector.

Four measurements of 300 s each were taken back to back. For each image, a region of 30×30 pixels was examined at coordinates $(260 : 290, 120 : 150)$, this region was chosen due to the lack of bad pixels and was assumed to be representative of the whole detector. The procedure described in Section 2.2 for the calculation of the QE was followed.

4 Results and Discussion

4.1 Simulated PSFs

Figure 9(a) is an example of the 'raw' output from the GATE simulations, while Figure 9(b) is the variation of the number of counts through the centre of the bright region in Figure 9(a). This particular example involved a 1 mm pinhole, with equal detector-collimator and collimator-source distances of 5 cm.

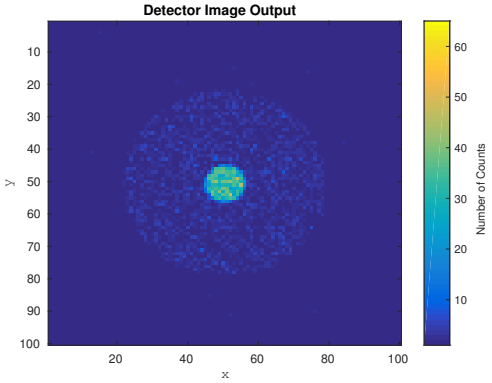

(a) Detector image of PSF measurement.

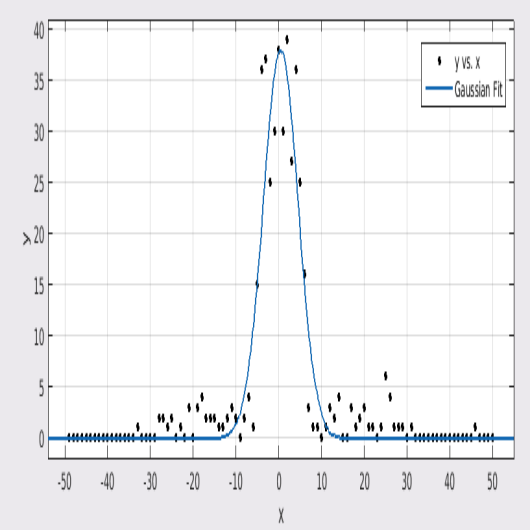

(b) The number of counts along y=50 of Figure 9(a) with a Gaussian fit.

Figure 9: Output from PSF measurements conducted in GATE, this example with a 1 mm pinhole at a detector-collimator distance of 5 cm, and a collimator-source distance of 5 cm.

The 'halo' around the central bright area in Figure 9(a) arises from the pinhole design, and the fact that there is less lead for the gammas to pass through around the pinhole. This effect leads to the two 'bumps' on either side of the central peak in Figure 9(b). Using Matlab, Gaussians were fitted to the integrated data (Figure 9(b)) for all pinholes and scenarios. The standard deviation was extracted to within a 95% confidence limit and used to calculate the FWHM. Figure 10 shows the FWHMs for all pinholes and distances, with their associated errors.

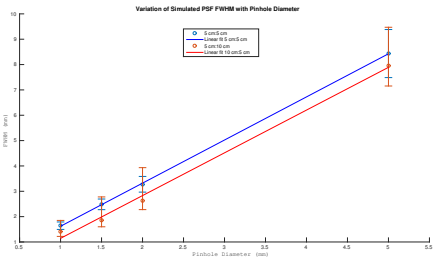

Figure 10: FWHMs of the simulated PSFs for varying pinhole diameters at collimator-source distances of 5 cm and 10 cm, with a detector-collimator distance of 5 cm. Blue linear fit: $y = 1.7x - 0.081$, red linear fit: $y = 1.7x - 0.54$.

Curiously, the spatial resolving capabilities of the system when the collimator-source distance is 10 cm and the magnification is $\frac{1}{2}$ is systematically superior to the situation in which the magnification is 1 and both distances are 5 cm. Also, the linear fits performed in Matlab assign equal gradients to the two data sets

which seems to contradict Equation 7 which suggests that the closer the source is to the pinhole, the better the resolution is. A possible explanation could be that the pinhole accepts more photons travelling at slightly larger angles when the source is at 5 cm as opposed to when it is at 10 cm, widening the FWHM of the PSF. Moreover, the uncertainties associated with the FWHM at a collimator-source distance of 10 cm are so large, that they encompass all FWHMs allowed by the uncertainties associated with the 5 cm system; the uncertainties are too high to be able to state with confidence that one system has a superior resolution to the other. It is clear from Figure 9b that running simulations with more photon histories would be useful, since not even the central peak is particularly smooth, affecting the Gaussian fit. The literature that validated the use of GATE for modelling PSFs through collimators with Tc-99m found that FWHM should increase with distance, but used a different collimator design [19], consisting of a "low energy high resolution collimator", a type of parallel hole collimator; they also generated 140 million photon histories each simulation, as opposed to the 100 million generated in these simulations.

4.2 Phantom Measurements and Binning

A small selection of the experimentally obtained phantom images is presented in this section, alongside the resulting image when different binning procedures are applied to them. The detector-collimator distance is always 4.5 cm.

4.2.1 Images obtained with 5.0 mm Pinhole

Figures 11 and 12 depict the image obtained of the phantom during a fast exposure of 5 s. An exposure of 1 s was tested at a source distance of 4.5 cm, too, and gave a similar result to that shown in Figure 11, with the exception that there were no significant signals in the binned image using the median method. At 4.5 cm, the 5 mm pinhole is just able to resolve the different rows of wells in the phantom, the centres of which are 10 mm away from each other. The edges of the wells in the bottom and middle rown are thus vertically separated by 8.5 mm, and the resolution of the 5 mm pinhole at 4 mm is better than or equal to 8.5 mm. Referring back to Figure 10, we see that the simulated PSF FWHM with these conditions is somewhere between 8 mm and 9 mm – a good agreement with the experimental data. At a source distance of 9.5 cm, however, the resolution is poorer than predicted and the 5 mm pinhole is unable to resolve the different rows of wells, imaging the phantom as a single region of counts.

The minimum binning method is of no use at such short exposures, it seems, seeing as the number of counts is so low. The median binning method provides less structure, but improves on the SNR compared to the mean, whilst the mean binning method enhances the intensity of the original image a little.

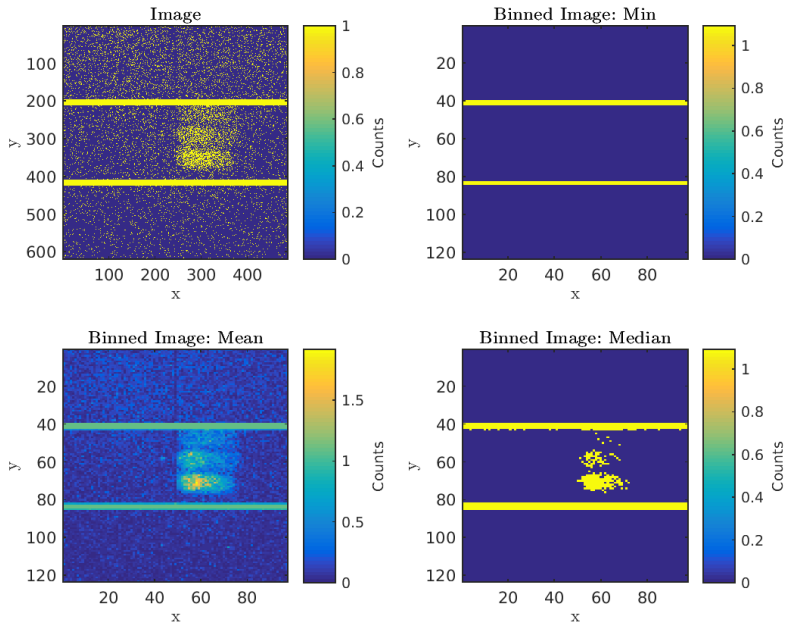

Figure 11: 5.0 mm pinhole at a distance of 4.5 cm from source. Exposure time = 5 s.

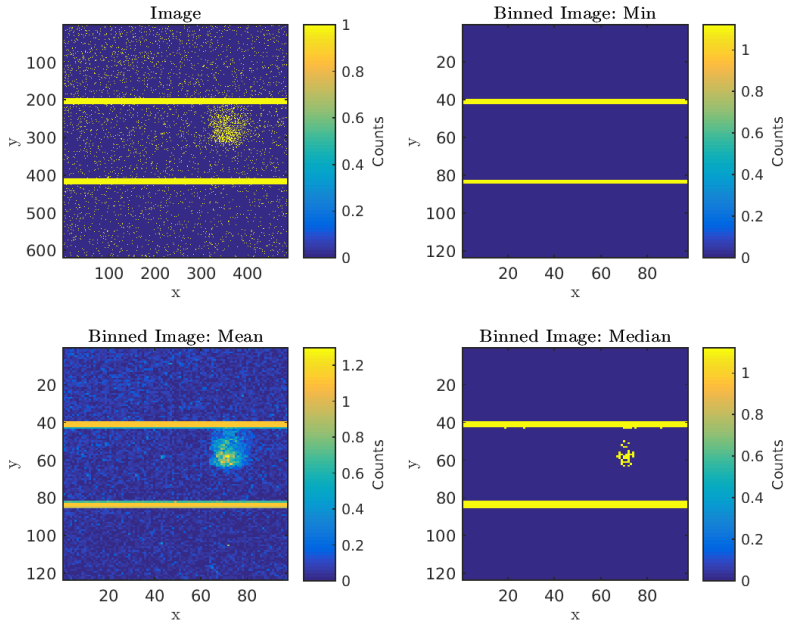

Figure 12: 5.0 mm pinhole at a distance of 9.5 cm from source. Exposure time = 5 s.

4.2.2 Images obtained with 2.0 mm Pinhole

The 2.0 mm pinhole shows significant improvements in resolution compared to the 5.0 mm pinhole as evident from Figures 13 and 14, but requires a longer exposure time to do so. At a source distance of 4.5 cm in Figure 13, the smallest resolvable distance seems to be the 3 mm gap between the third and fourth well in the first row clearly visible in the original image and the mean binned image. A resolution of just over 3 mm was predicted for this scenario. Once more, the experimental results at a distance of 4.5 cm are in agreement with the simulations. At a distance of 9.5 cm, the sensitivity drops and as does the resolution. The rows of the phantom wells are evidently distinguishable from each other, but the individual wells are not.

It is possible that the exposure time was too low at a distance of 9.5 cm to be able to resolve the individual phantom wells, and further images with longer exposures confirm that increasing the exposure time to 120 s reveals some more structure.

Similarly to the case with the 5.0 mm pinhole, the min binning method shows no signal, the median binning method increases SNR, but distorts detail and the mean binning method has the advantage that it seems to intensify and enhance the original image.

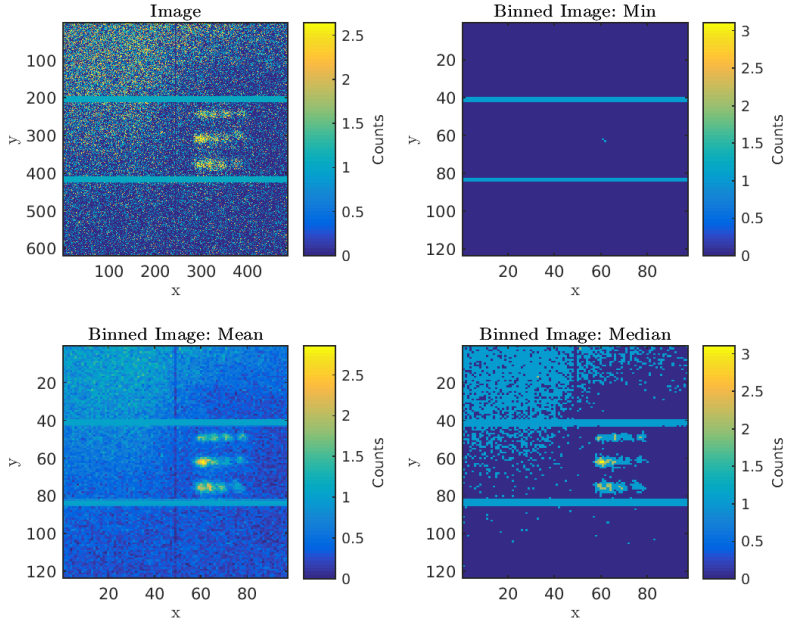

Figure 13: 2.0 mm pinhole at a distance of 4.5 cm from source. Exposure time = 30 s.

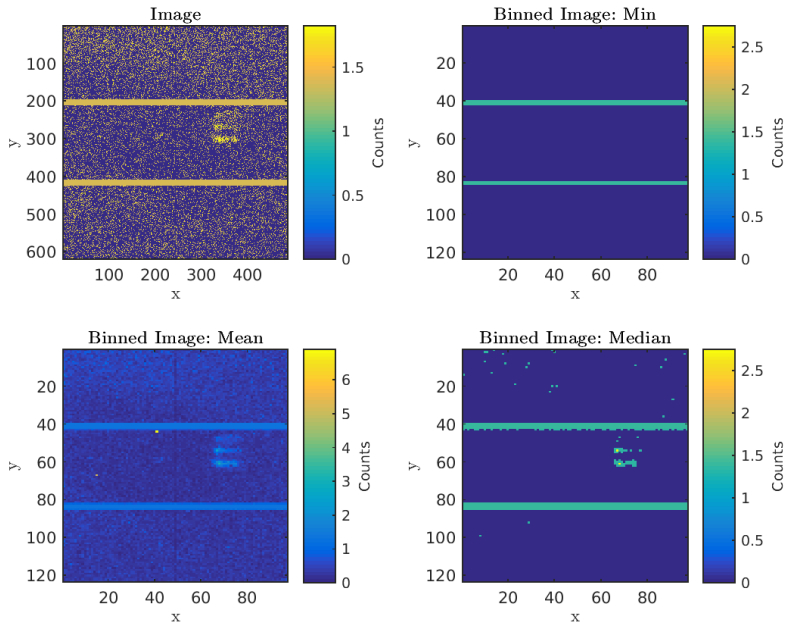

Figure 14: 2.0 mm pinhole at a distance of 9.5 cm from source. Exposure time = 30 s.

4.2.3 Images obtained with 1.5 mm Pinhole

The 60 s exposure in Figure 15 with the 1.5 mm pinhole indicates that the resolution of the system is close to 2 mm, since the second and third wells of the bottom row are almost distinguishable from each other at a source distance of 4.5 cm. At 9.5 cm in Figure 16, the three rows of the phantom are visible, and some structure can be seen in the original image in the bottom row, but resolution is around 3mm, judging by ability to distinguish the third and fourth wells in the bottom row from each other.

The mean binning method appears to have no benefit at 4.5 cm, with the median binning method being most useful at a source distance of 9.5 cm, as it eliminates a lot of noise.

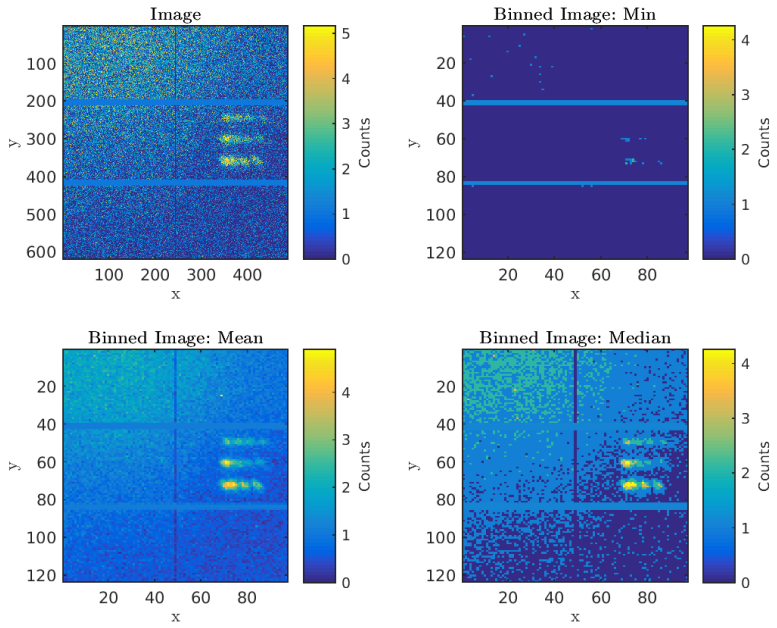

Figure 15: 1.5 mm pinhole at a distance of 4.5 cm from source. Exposure time = 60 s.

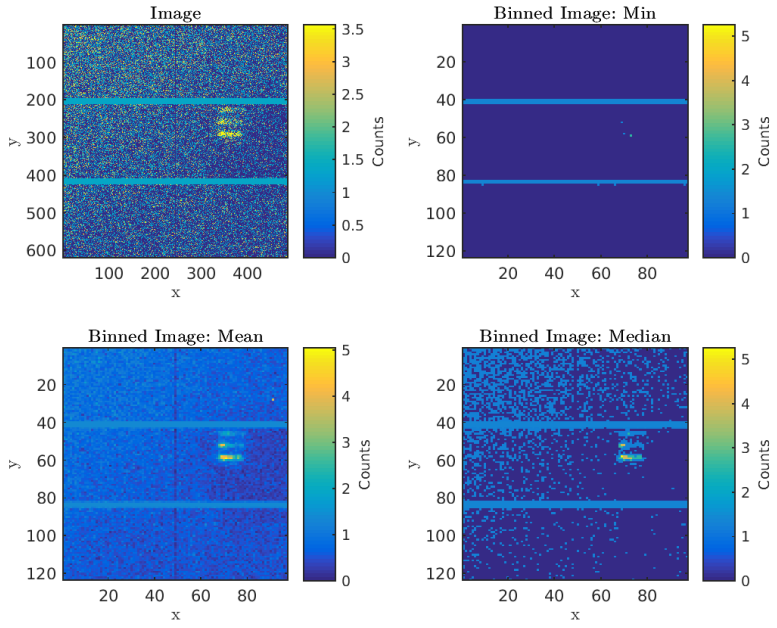

Figure 16: 1.5 mm pinhole at a distance of 9.5 cm from source. Exposure time = 60 s.

4.2.4 Images obtained with 1.0 mm Pinhole

As shown in Figures 17 and 18, long exposure images with the 1 mm pinhole provide superior resolution in comparison to the other imaging systems. At 4.5 cm in Figure 17, the two first wells in the bottom row that are separated by 1 mm are clearly visible, and resolution is on the sub millimetre scale. The predicted value for detector-collimator and collimator-source distances of 5 cm was around 1 mm, in line with the experimental findings. Figure 18 reveals some structure in the bottom row of the phantom at a 9.5 cm source distance, indicating a resolution on the order of a couple of millimetres.

In Figures 17 and 18, the mean binning technique is the most useful as it intensifies the original image. It does, however, also increase the background. The other two techniques either distort the image somewhat, or leave too little to be seen.

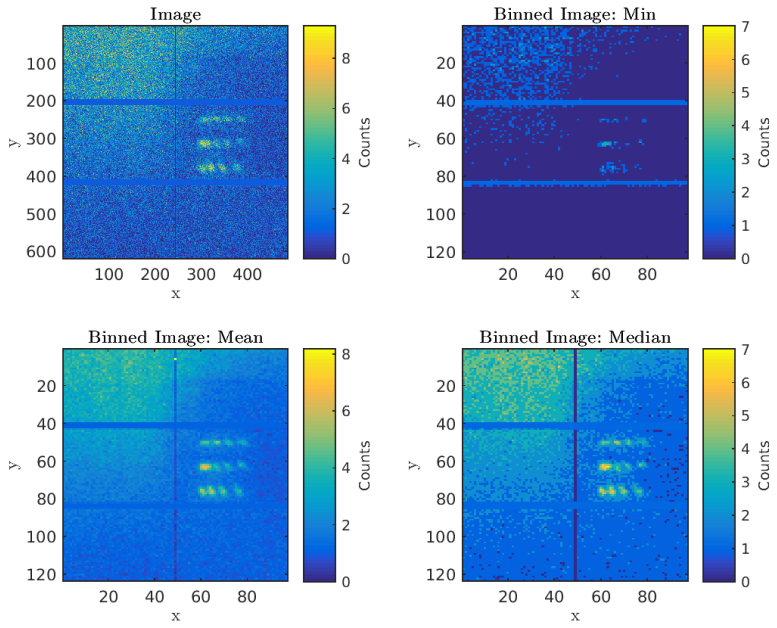

Figure 17: 1.0 mm pinhole at a distance of 4.5 cm from source. Exposure time = 120 s.

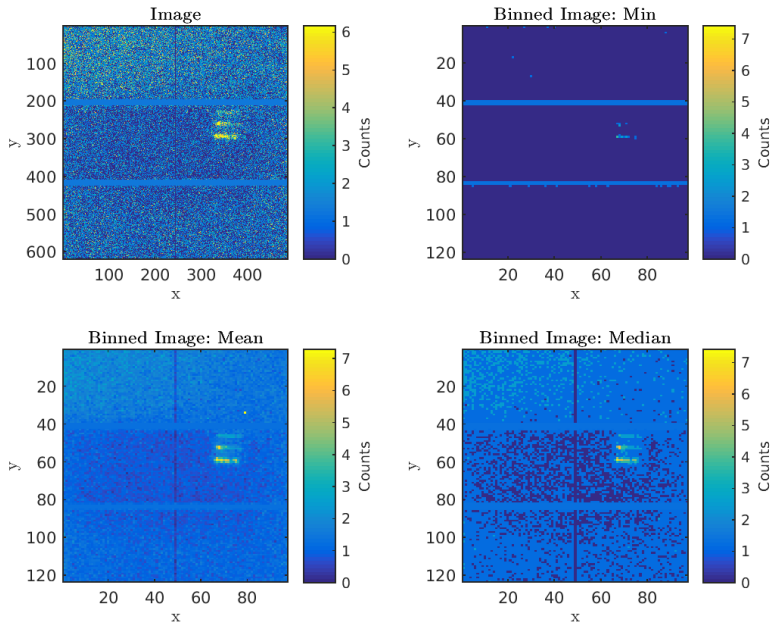

Figure 18: 1.0 mm pinhole at a distance of 9.5 cm from source. Exposure time = 120 s.

4.2.5 Discussion on Phantom Images and Binning Method

The total activity in the phantom was 26.9 MBq, divided between all wells. All phantom images have been corrected to this value, as explained in Section 3.3. This represents a similar dose to what a patient would receive during existing SNB procedures, and the images therefore somewhat realistically represent what the output would be during the procedure.

For the context of real time SNB, upon intial injection of the dose, a larger pinhole is more suitable if images are to be taken with short exposure times. Use of the 5 mm pinhole at a distance of 5 cm would allow the surgeon to track the path of the radiotracer in 5 s exposures, and resolve structures that are 8.7 mm apart. The fact that it provides a clear signal at a source distance of 10 cm suggests that it could also be used as a tool to initially localise the relevant structures. For a detailed image, it would be optimal to be able to switch to the 2.0 mm pinhole intraoperatively. The 2.0 mm imaged almost all structure in the phantom at an exposure time of 30 seconds and a resolution of 3 mm from 4.5 cm away, giving the surgeon a detailed map of the lymph node locations. The resolution for the smallest pinhole (2.5 mm) available for the Sentinella 102 mentioned in Section 1 at a source distance of 5 cm is cited as 5.4 mm and its sensitivity is 110 cpm/μCi [21]. That is to say – a 30 s exposure to the phantom with the gamma cammera, Sentinella 102, would result in 41 counts at a resolution of 5.4 mm. The 2.0 mm pinhole combined with the PILATUS3 CdTe achieved greater than 41 counts in the encompassing region of the phantom, and managed a higher resolution, suggesting that the detector indeed would be suitable for intraoperative SNB.

The discussion above takes no consideration to the fact that these experiments were conducted in air, whereas tracking of a radiotracer during SNB would involve measurements through body tissue. Assuming that the tissue has a composition similar to that of water, there would be a lot more scattering and attenuation of photons, leading to images of poorer quality.

The binning methods acted in different ways. The mean binning method smoothed out the image, while the median sometimes managed to clear noise, but distorted the image. The minimum binning method did not often show signal, presumably due to the low incoming photon flux and requires a stronger signal to act beneficially. Although the mean binning method seemed to enhance the image, the risk is that any hot

pixels disrupt the whole scale, a small example of which can be seen in Figure 14 where a few pixels with a higher value cause a colour scale shift. If applied to any imaging system, however, algorithms can be written to counteract this. It is possible that the median binning method would find more application if the experiments were conducted in a medium in which the photons would scatter more than in air, for example in water. A quantitative comparison of the effects of the different binning methods on the SNR could be useful, perhaps by choosing two points in every image and simply comparing the intensities of the two, or by plotting the intensity across one row of the well. There are also other image processing techniques that could be useful; a fast fourier transform, for example, could be applied to remove noise. This might require some more computation time, and the processing could not be done in real time in the same way as the other binning methods, but it could prove to be a useful tool.

4.3 Quantum Efficiency

The average, absolute QE calculated for the PILATUS3 CdTe detector at 140.5 keV was $(20.8 \pm 0.2)\%$; an outstanding result when considering that other semiconductor detectors such as Silicon have the same QE at 20 keV. Although the relative uncertainty in the measurement is small, and the separate measurements of QE differed very little from each other, the QE should be investigated over larger regions on the detector face and at different incoming photon fluxes.

5 Conclusion and Outlook

Preliminary experiments have been done to show that the PILATUS3 CdTe shows promise as a real-time intraoperative imaging device during sentinel lymph node biopsy, to guide surgeons to the relevant lymph nodes, and also to track the passage of the radiotracer injected during such procedures. Its resolving capabilities and sensitivity coupled with a 2.0 mm pinhole already surpass those of existing technologies in hospitals for the same purpose, such as the Sentinella 102.

Modelling of the point spread functions for PILATUS3 images through pinholes of varying diameter confirmed that the decrease in spatial resolution is linear with increase in aperture on the scales examined. The unusual result that a collimator-source distance of 10 cm resulted in higher resolution (lower FWHM of the PSF) than a collimator-source distance of 5 cm, both for the detector-collimator distance 5 cm, should be further probed and is potentially due to the high uncertainties associated with the FWHMs. The agreement of the simulated resolution for the 5cm : 5cm case with the experimental data is, however, reassuring and suggests that further simulations in GATE would also be representative of experimental results.

The quantum efficiency of the PILATUS3 CdTe detector has not been measured previously at 140.5 keV, and the value of $(20.8 \pm 0.2)\%$ determined in these experiments far outshines the quantum efficiency of the more common silicon semiconductor detector at the same energy.

The general results are promising, but in order for the PILATUS3 CdTe to find application as a real time camera during SNB, more research into the behaviour of the imaging system is required. First and foremost, simulations should be run in GATE with a phantom and in a tissue-like medium to evaluate the effect of scattering and attenuation of the photons. Secondly, optimisation of the collimator design is required. In this thesis, four different pinhole apertures and two different collimator-source distances have been tested. More tests varying the channel depth of the pinhole and its placement could be conducted to find the optimal resolution-sensitivity compromise. Different collimator designs could be tested altogether, to see if constructions such as a parallel hole collimator, or a multi-pinhole collimator, are more suited for the purpose.

Further experiments not included in the report were performed on the PILATUS3 CdTe, and may be the subject of a publication together with the results from this thesis. These experiments include characterising the detector response to a uniform flux of photons over its surface, and also SPECT measurements on the phantom, to ascertain whether or not the imaging system can produce three dimensional images of high resolution. Investigations into SPECT with CdTe detectors have showed potential, with the high energy resolution of CdTe sensors giving better contrast in images due to scatter rejection [22].

Acknowledgements

There are many I would like to thank for their support and dedication to making this project possible. My supervisor, Dr. Roger Rassool, for his guidance, enthusiasm, and for teaching and showing me much more than what the project alone encompassed. I would like to thank Dr. David Peake and Dr. Bryn Sobott for their helpful discussions and the time that they took in helping me. The PhD students, Thomas Lucas and Paul Giansiracusa, for their endless patience and for all the fun times we had in the lab. Lastly, I would like to thank Graeme O'Keefe and David Thomas of the department for Nuclear Medicine at the Austin Hospital for so kindly providing me with the isotopes required to complete the work.

References

[1] Moncayo, V. M., J. N. Aarsvold, and N. P. Alazraki. "Lymphoscintigraphy and Sentinel Nodes." *Journal of Nuclear Medicine* 56.6 (2015): 901-07.

[2] Bree, Remco De, and Omgo E. Nieweg. "The History of Sentinel Node Biopsy in Head and Neck Cancer: From Visualization of Lymphatic Vessels to Sentinel Nodes." *Oral Oncology* 51.9 (2015): 819-23.

[3] Monroe, Marcus M., and Stephen Y. Lai. "Sentinel Lymph Node Biopsy for Oral Cancer: Supporting Evidence and Recent Novel Developments." *Current Oncology Reports* 16.5 (2014)

[4] Nieweg OE, Tanis PJ, Kroon BBR. The definition of a sentinel node. *Ann Surg Oncol* 2001;9:538–41.

[5] Surasi, D. S., J. O'malley, and P. Bhambhvani. "99mTc-Tilmanocept: A Novel Molecular Agent for Lymphatic Mapping and Sentinel Lymph Node Localization." *Journal of Nuclear Medicine Technology* 43.2 (2015): 87-91

[6] Browne, E., and J.k. Tuli. "Nuclear Data Sheets for A = 99." Nuclear Data Sheets 112.2 (2011): 275-446

[7] "Sentinella 102." Oncovision GEM-Imaging SA. N.p., n.d. Web. 29 Aug. 2015. [http://www.gem-imaging.com/productos/sentinella102/sentinella102.php]

[8] Giammarile, Francesco, Naomi Alazraki, John N. Aarsvold, Riccardo A. Audisio, Edwin Glass, Sandra F. Grant, Jolanta Kunikowska, Marjut Leidenius, Valeria M. Moncayo, Roger F. Uren, Wim J. G. Oyen, Renato A. Valdés Olmos, and Sergi Vidal Sicart. "The EANM and SNMMI Practice Guideline for Lymphoscintigraphy and Sentinel Node Localization in Breast Cancer." *European Journal of Nuclear Medicine and Molecular Imaging* 40.12 (2013): 1932-947

[9] References Lymphoseek Injection. Prescribing information. Dublin, OH: Navidea Biopharmaceuticals, Inc.; September 2014

[10] Li, Li, Shiro Mori, Maya Sakamoto, Shoki Takahashi, and Tetsuya Kodama. "Mouse Model of Lymph Node Metastasis via Afferent Lymphatic Vessels for Development of Imaging Modalities." *PLoS ONE* 8.2 (2013)

[11] Darambara D. G. and Todd-Pokropek, A., Solid state detectors in nuclear medicine. *Q J Nucl Med* 46: 3-7 (2002)

[12] Technical Specification and Operating Procedure. PILATUS3 300K 500Hz Detector System. Version: V2.1. Dectris.

[13] "Cadmium Telluride Sensors for Hard X-Ray Detection." Dectris. N.p., n.d. Web. 27 Aug. 2015. [https://www.dectris.com/cdte-sensors.html#main_head_navigation].

[14] "Hybrid Pixel" Dectris. N.p., n.d. Web. 27 Aug. 2015. [https://www.dectris.com/cdte-sensors.html#main_head_navigation].

[15] "Instant Retrigger Technology". Dectris. N.p., n.d. Web. 27 Aug. 2015. [https://www.dectris.com/cdte-sensors.html#main_head_navigation].

[16] Zaluzec, Nestor J. "Analytical Formulae for Calculation of X-Ray Detector Solid Angles in the Scanning and Scanning/Transmission Analytical Electron Microscope." *Microscopy and Microanalysis* 20.04 (2014): 1318-326.

[17] References Rossmann, Kurt. "Point Spread-Function, Line Spread-Function, and Modulation Transfer Function." *Radiology* 93.2 (1969): 257-72.

[18] "Setting up the Physics." GATE Users Guide V7.0. OpenGATE Collaboration, 15 July 2014. Web. 27 Aug. 2015. [http://wiki.opengatecollaboration.org/index.php/Users_Guide_V7.0:Setting_up_the_physics]

[19] Lazaro, D., I. Buvat, G. Loudos, D. Strul, G. Santin, N. Giokaris, D. Donnarieix, L. Maigne, V. Spanoudaki, S. Styliaris, S. Staelens, and V. Breton. "Validation of the GATE Monte Carlo Simulation Platform for Modelling a CsI(Tl) Scintillation Camera Dedicated to Small-animal Imaging." *Physics in Medicine and Biology* 49.2 (2004): 271-85

[20] Connolly, L. P., S. T. Treves, S. A. Connolly, R. E. Zimmerman, Z. Bar-Sever, D. Itrato, and R. T. Davis. "Pediatric Skeletal Scintigraphy: Applications of Pinhole Magnification." *RadioGraphics* 18.2 (1998): 341-51

[21] Quality Control Kit for Gamma Camera Sentinella 102. Users Manual. Oncovision GEM-Imaging SA. Rev.4 01/04/2009:20.

[22] Tsuchiya K, Takahashi I, Kawaguchi T, Yokoi K, Morimoto Y, Ishitsu T, et al. Basic performance and stability of a CdTe solidstate detector panel. *Ann Nucl Med.* 2010;24:301–11.

Appendix

A Photographs of Experimental Setup

Figure 19: Preparing for a quantum efficiency measurement. The PILATUS3 CdTe with shield on is visible on the optical bench, along with the stage and perpspec vial holder used to keep the vial with source in place. Lead shielding not in place at this point.

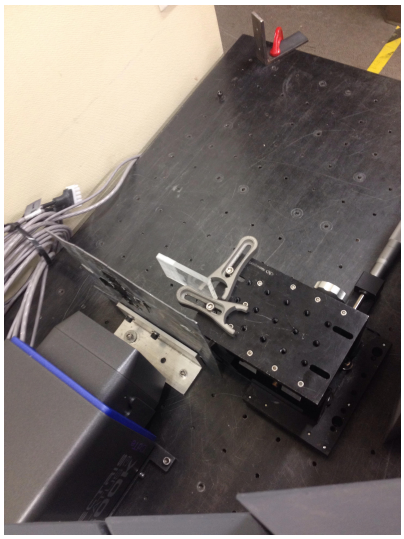

Figure 20: Top view of the phantom in its holder and the detector-collimator arrangement.